OPEN ACCESS
Journal of Astronomical Instrumentation, Vol. 11, No. 2 (2022) 2250010 (21 pages)

DOI: 10.1142/S2251171722500106

World Scientific
www.worldscientific.com

The Marshall Grazing Incidence X-ray Spectrometer (*MaGIXS*)

P. R. Champey[1,*], A. R. Winebarger[1], K. Kobayashi[1], P. S. Athiray[1,2], E. Hertz[3], S. Savage[1], B. Beabout[1], D. Beabout[1], D. Broadway[1], A. R. Bruccoleri[4], P. Cheimets[3], J. Davis[1], J. Duffy[1], L. Golub[3], D. A. Gregory[5], C. Griffith[1], H. Haight[1], R. K. Heilmann[6], B. Hogue[1], J. Hohl[3], D. Hyde[1], J. Kegley[1], J. Kolodzieczjak[1], B. Ramsey[1], J. Ranganathan[1,2], B. Robertson[1], M. L. Schattenburg[6], C. O. Speegle[1], G. Vigil[1], R. Walsh[7], B. Weddenorf[8] and E. Wright[1]

[1]NASA George C. Marshall Space Flight Center, Huntsville, AL 35812

[2]Center for Space Plasma and Aeronomic Research
University of Alabama in Huntsville, AL 35899, USA

[3]Center for Astrophysics – Harvard & Smithsonian, Cambridge, MA 02138

[4]Izentis LLC, Cambridge, MA 02139

[5]Department of Physics, University of Alabama in Huntsville, Huntsville, AL 35899

[6]Massachusetts Institute of Technology, Cambridge, MA 02139

[7]University of Central Lancashire, Preston, PR1 2HE, UK

[8]Weddendorf Design, Inc., Huntsville, AL 35803

*patrick.r.champey@nasa.gov

Received March 4, 2022; Revised April 13, 2022; Accepted April 13, 2022; Published June 15, 2022

The Marshall Grazing Incidence X-ray Spectrometer (*MaGIXS*) is a sounding rocket instrument that flew on July 30, 2021 from the White Sands Missile Range, NM. The instrument was designed to address specific science questions that require differential emission measures of the solar soft X-ray spectrum from 6 – 25 Å(0.5 – 2.1 keV). *MaGIXS* comprises a Wolter-I telescope, a slit-jaw imaging system, an identical pair of grazing incidence paraboloid mirrors, a planar grating and a CCD camera. While implementing this design, some limitations were encountered in the production of the X-ray mirrors, which ended up as a catalyst for the development of a deterministic polishing approach and an improved meteorological technique that utilizes a computer-generated hologram (CGH). The opto-mechanical design approach addressed the need to have adjustable and highly repeatable interfaces to allow for the complex alignment between the optical sub-assemblies. The alignment techniques employed when mounting the mirrors and throughout instrument integration and end-to-end testing are discussed. Also presented are spatial resolution measurements of the end-to-end point-spread-function that were obtained during testing in the X-ray Cryogenic Facility (XRCF) at NASA Marshall Space Flight Center. Lastly, unresolved issues and off-nominal performance are discussed.

Keywords: Soft X-ray spectrometer; imaging spectrometer; solar spectroscopy; optical fabrication; optical alignment; X-ray testing.

1. Introduction

Since the earliest sounding rocket flights in the 1940s, ultraviolet (UV), extreme ultraviolet (EUV), and X-ray spectral observations have been used to measure physical properties of the solar atmosphere. During this time, there has been substantial improvement in the spectral, spatial, and temporal resolution of the observations in the UV and EUV wavelength ranges. At wavelengths shorter than 100 Å, however, observations of the solar corona with simultaneous spatial and spectral resolution are limited, and not since the late 1970s have

*Corresponding author.

spatially resolved solar X-ray spectra been measured (Doschek & Feldman, 2010). Nonetheless, X-ray spectroscopy has unprecedented potential for providing unique capabilities for answering fundamental questions in solar physics (Del Zanna *et al.*, 2021; Young, 2021). Soft X-ray (SXR) wavelengths are notably dominated by emission lines formed at high temperatures, and spectroscopic information from this regime is an untapped resource for probing highly energetic physical processes that have been largely inaccessible.

The Marshall Grazing Incidence X-ray Spectrometer (*MaGIXS*) is an instrument that was designed in response to this critical gap in solar observations and packaged for testing as a sounding rocket payload. Using X-ray spectroscopic techniques implementing a series of finely polished grazing incidence mirrors, in combination with a specially designed grazing incidence grating with varied line spacing, *MaGIXS* is capable of measuring the solar spectrum from 6 – 25 Å (0.5 – 2.1 keV) with both spatial and spectral resolutions. As a sounding rocket mission, the powerful set of plasma diagnostics provided by *MaGIXS* addresses a long-standing question in solar physics concerning the nature of coronal heating in active region structures (Athiray *et al.*, 2019). Table 1 lists the instrument requirements derived from the mission science that will be presented in Savage *et al.* (2022).

The wavelength band selected for *MaGIXS* includes strong emission lines formed in the temperature range of interest, as shown in Table 2.

Table 1. Key proposed science and instrument requirements.

Science requirement	Instrument requirement
Observe emission lines formed by 3–10 MK plasma formed by a variety of elements	Observe 6 – 25 Å (0.5 – 2.1 keV)
Spectrally resolve strong emission lines	Spectral resolution < 100 mÅ
Spatially resolve unique active region structures	Spatial resolution $< 6''$
Have adequate effective area to make a definitive measurement after summing 300 s of data acquired during a sounding rocket flight	Effective area $> 1 \times 10^{-3}$ cm^2
Have adequate cadence to accommodate a short enough exposure so that the brightest lines do not saturate the detector	Cadence < 10 s

Table 2. Key emission lines in the *MaGIXS* spectral range, ordered by increasing wavelength.

Spectral line	Wavelength [Å]	Energy [keV]	Log maximum temp
Mg XII	8.42	1.47	7.0
Mg XI	9.16	1.35	6.8
Ne X	12.13	1.02	6.75
Fe XX	12.83	0.96	7.05
Ne IX	13.45	0.92	6.6
Fe XIX	13.52	0.92	6.95
Fe XVIII	14.20	0.87	6.9
Fe XVII	15.01	0.83	6.75
Fe XVII	15.26	0.81	6.75
O VIII	16.00	0.78	6.5
Fe XVII	16.78	0.74	6.75
Fe XVII	17.05	0.73	6.75
Fe XVIII	17.62	0.71	6.9
O VIII	18.97	0.65	6.5
O VII	21.6	0.57	6.3
N VII	24.8	0.50	6.3

Figure 1 shows the emissivity functions ($G(T)$) for these spectral lines derived using CHIANTI atomic database version 9.0.1 assuming coronal abundances (Schmelz *et al.*, 2012) and the standard CHIANTI ionization equilibrium (Del Zanna *et al.*, 2015). The spectral resolution goal is driven by the desire to separate the Fe XVII 17.05 Åline from the Fe XVIII 17.62 Åline. The effective area requirement is derived from calculating predicted count rates in this wavelength range, as described in detail in Athiray *et al.* (2021), to provide the signal-to-noise ratio needed for the spectroscopic analysis after summing the data over the ∼300 s sounding rocket flight. The exposure duration is set so the brightest lines in this wavelength range will not saturate the detector.

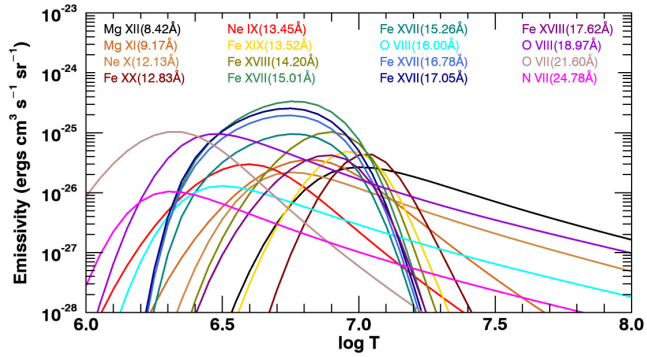

Fig. 1. The emissivity functions of the *MaGIXS* spectral lines listed in Table 2, calculated using CHIANTI atomic database version 9.0.1 with coronal abundances (Schmelz *et al.*, 2012) and ionization equilibrium (Del Zanna *et al.*, 2015).

This paper provides a technical overview of the *MaGIXS* instrument and discusses the motivations for the optical design and mirror fabrication, the opto-mechanical design and alignment approach, and measurements of the spatial component of the point-spread-function of fully integrated instrument. The instrument calibration, which was carried out in parallel to the optical alignment, has been reported in Athiray *et al.* (2020, 2021), henceforth referred to as Calibration I and Calibration II, respectively.

The most challenging aspect when developing the *MaGIXS* instrument was achieving the high spatial and spectral resolution requirements given in Table 1. The resolution requirements acted as a forcing function to develop and implement new techniques in grazing incidence mirror and grating fabrication. They also drove the design of the mechanical structures (optical bench, mirror mounts, mechanical interfaces) and subsequent fabrication methods. Despite these advancements in fabrication and the sophisticated opto-mechanical design, *MaGIXS* did not achieve these resolution requirements; however, the progress made on the development of fabrication and alignment techniques has paved the way for future instruments.

2. Technical Approach

The *MaGIXS* instrument consists of a grazing incidence telescope and spectrometer with a CCD camera, slit-jaw context imager, and avionics. It was designed to be housed in a 17-inch diameter rocket skin and flown aboard a two-stage Terrier-Black Brant sounding rocket. *MaGIXS* is an MSFC-led experiment, with partners from the Smithsonian Astrophysical Observatory (SAO), the Massachusetts Institute of Technology (MIT), Izentis LLC, and the University of Central Lancashire (UCLan).

2.1. *Optical design*

The *MaGIXS* optical design is driven by the need for fine spatial and spectral resolutions over a medium-sized active region ($\approx 6'$ FOV, Warren *et al.* (2012)), packaged inside of a standard sounding rocket experiment volume. The most basic design requirements called for a focusing optic, dispersive and re-imaging elements, and a detector. Given the resolution specifications over the field of view, the optical system needed to exhibit minimized astigmatism, coma and field curvature for off-axis imaging. Several optical design concepts were considered for *MaGIXS* and those are discussed in Kobayashi *et al.* (2010). Ultimately, the design settled on a Wolter-I telescope feeding a spectrometer comprised of a finite conjugate mirror pair and a planar grating, and a low-noise CCD camera. Figure 2 shows the layout of the optical design, while Table 3 provides system and component-level properties. The ray trace model for this design produced an intrinsic $5.6''$ angular and 22 mÅ spectral resolution.

The original optical design included a narrow slit ($2.8''$ ($15\,\mu$m) wide $\times 8'$ (2.5 mm) long) at the telescope focal plane; however, after calibration was concluded the slit was replaced by a $12'$ (3.84 mm) wide $\times 33'$ (10.6 mm) long slot. This modification was motivated by the lower than expected count rates, as described in Calibration II, Sec. 2.2. Increasing the size of the field stop converted the instrument from a slit to a slit-less imaging spectrometer, which produces spatially and spectrally overlapped images.

2.1.1. *Wolter-I telescope*

The Wolter-I telescope consists of a paraboloid primary and a hyperboloid secondary mirror in a co-axial arrangement on a single contiguous substrate (Wolter, 1952; van Speybroeck & Chase, 1972). A Wolter-I prescription was chosen because of its well-studied on- and off-axis imaging performance, and also because of production heritage at MSFC (O'Dell *et al.*, 2015). The telescope mirror was a single, thin-shell nickel–cobalt replicated optic. This particular Wolter-I design is reasonably fast (f/7.2),

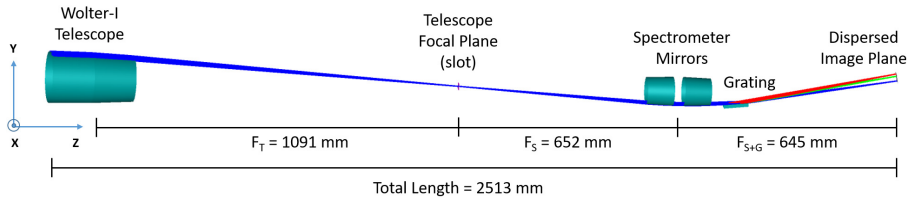

Fig. 2. The *MaGIXS* optical layout.

Table 3. Optical system, components, and their properties.

Category	Parameter	Value
Observation	Wavelength range	6 – 25 Å
	Energy range	0.5 – 2.1 keV
	Field of view (observed)	$33' \times 12'(28.83' \times 3.73')$
Entrance Filters	Type	150 nm Al on 70 lines per inch Ni mesh
Telescope	Type	Wolter-I
	Focal length	1.09 m
	Intersection radius	73.06 mm
	Substrate (thickness)	Replicated Ni-Co (1 mm)
	Coating (thickness)	Iridium (10 nm)
	Measured HPD (active aperture)[a]	16″
Spectrometer Mirrors (×2)	Type	Paraboloid
	Focal length	0.652 m
	Radius (max.; min.)	41.91 mm; 39.21 mm
	Substrate (thickness)	Replicated Ni-Co (1 mm)
	Coating (thickness)	Iridium (10 nm)
	Measured HPD (active aperture)[a]	17″
Grating	Type	Reflective, planar, varied-line-space
	Substrate (thickness)	Monocrystalline silicon (10 mm)
	Coating (thickness)	Iridium (10 nm)
	Measured efficiency (1st order)	14% at 12.50 Å(0.99 keV)
Focal Plane Filter	Type	150 nm Al on 200 nm of polyimide
Detector	Type	2 k × 1 k frame transfer CCD
	Pixel size	15 μm
	Plate scale (spatial; spectral)	2.8″/pixel; 11 mÅ/pixel
Instrument Performance	Angular resolution (HPD)[b]	28″ – 30″ (spatial component)
	Spectral Resolution	150 mÅ
	Resolving Power	74 – 98 ($\lambda/\Delta\lambda$) at 9.88 Å– 14.55 Å
	Effective area	0.005 cm^2 at 12.25 Å(1.01 keV)

Notes: [a]The active aperture is the 34° sub-aperture incident on the planar grating.
[b]Angular resolution in the spatial (cross-dispersion) axis.

which means the prescription calls for a steeper cone angle, and larger sag (departure from a cone) than, for example, telescopes that flew aboard *ART-XC* (Gubarev *et al.*, 2013, 2014), *FOXSI* (Krucker *et al.*, 2013; Christe *et al.*, 2016), and *IXPE* (O'Dell *et al.*, 2018; Ramsey *et al.*, 2019). The graze angle at the intersection plane is 0.96°, which meets the criteria for total external reflection across the 0.5 – 2.1 keV energy range. Additional telescope mirror properties are listed in Table 3.

2.1.2. *Spectrometer mirrors*

The spectrometer mirror design was optimized to reduce off-axis aberrations. The finite conjugate arrangement of the single-paraboloid spectrometer mirror pair meets the Abbé sine condition, which implies stigmatic imaging and significantly reduced coma. The first spectrometer mirror (SM1) lies confocal with the telescope mirror, while the second spectrometer mirror (SM2) focuses on the collimated beam from SM1. Both SM1 and SM2 were replicated from a common mandrel. Physical properties of the spectrometer mirrors are provided in Table 3.

2.1.3. *Grating*

The grating is a silicon substrate with a highly chirped varied line-space ruling, located down stream of SM2. The grating disperses the converging rays from SM2 to the CCD detector. The grating was designed using *Zemax OpticStudio* and the line period and line frequency are provided in Table 4. The varied line space (VLS) planar diffraction grating, fabricated by Izentis LLC, operates at a 2° graze angle, with a 1.6° blazed line profile. The grating was fabricated by way of a direct-write,

Table 4. Grating ruling.

y [mm]	Period: $\frac{1}{T}$ [nm]	Frequency: T [lines/mm]
32	541.6	1846.5
0	476.19	2100.0
−32	415.01	2409.6
−41	398.45	2509.7

E-beam lithography process onto a 10 mm thick silicon substrate. The silicon substrate was cut so that the orientation of the crystal plane (with respect to the cut surface) having Miller index = {111} matched the prescribed blaze angle. The {111} Miller index refers to the plane that crosses the *X, Y, Z* axes of a crystal at an intercept = 1. During the etching process, the {111} crystal face is etched at quicker rate, resulting in a saw-tooth (blazed) pattern. The grating was coated with a 10 nm thick layer of iridium at MSFC. The first- and second-order diffraction efficiencies were measured using the Advanced Light Source beam line 6.3.2 at Lawrence Berkeley National Laboratory (LBNL). The first-order efficiency at 12.25 Å(1.01 keV) is 14%. The full set of measurements are reported in Calibration II (Sec. 4.6.1 & Fig. 11). A paper on the *MaGIXS* grating development, fabrication, and efficiency measurements will be prepared at a later date.

2.1.4. *CCD camera*

The *MaGIXS* science camera is a second generation MSFC-developed camera with lineage from the *Chromospheric Lyman-Alpha Spectro-Polarimeter* (CLASP; Champey *et al.*, 2014, 2015), and is a reconfigured version of the *High-Resolution Coronal Imager* re-flight (Hi-C 2.0/2.1) camera (Rachmeler *et al.*, 2019). The primary difference between the Hi-C 2.0/2.1 and *MaGIXS* camera is the mode of operation.

The *MaGIXS* science camera uses a CCD230-42 back-illuminated, astro-processed, un-coated sensor manufactured by Teledyne e2v. This sensor is a 20 48 × 2064 pixel array, with 15 μm square pixels. The detector is operated in frame transfer mode, meaning the central 2048 × 1024 region is the active light-collecting region, while the remaining 2048 × 1040 pixels are divided into two, mechanically masked storage regions. When a new image is initiated, the stored charge in the light-collecting region is shifted to the storage regions of the sensor to be read out, while the active region continues to integrate.

The CCD is passively cooled to maintain a temperature below −65°C during observations to minimize the dark current (thermal noise). During operation in vacuum, liquid nitrogen (LN2) is pumped into the payload and through a copper block (cold reservoir) that is connected to the copper CCD holder via an electrically isolated bundle of braided copper strands. The cold reservoir is cooled to −125°C in order to have adequate thermal mass to maintain the CCD temperature set point of −65°C throughout operation. Figure 3 shows a CAD model of the *MaGIXS* camera and the braided copper cold strap.

2.1.5. *Entrance and focal plane filters*

There are two sets of filters for blocking visible and UV light — one set at the entrance aperture of the telescope and a single focal plane filter in front of the CCD detector. The entrance filter is 150 nm of Al on 70 lines per inch nickel mesh, the same design is utilized for several of the EUV filters on the *Atmospheric Imaging Assembly* (AIA) that is aboard the *Solar Dynamics Observatory* (SDO; Lemen *et al.*, 2012). The focal plane filter is 150 nm Al deposited on a 200 nm polyimide substrate, similar to Al-poly filter on the *X-ray Telescope* (XRT) aboard *Hinode* (Golub *et al.*, 2007). Both sets of filters are supported by custom designed

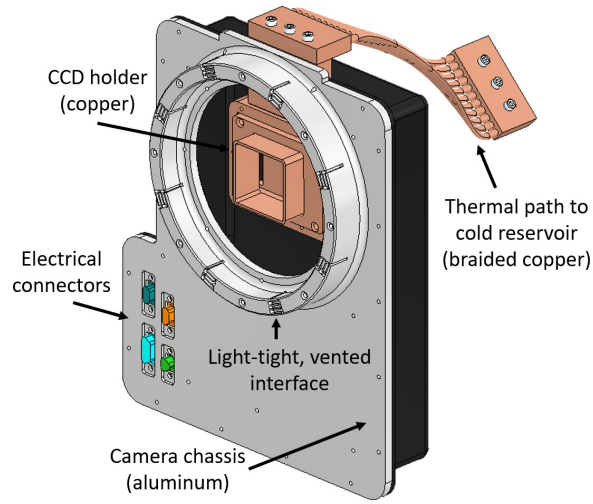

Fig. 3. A CAD model of the *MaGIXS* camera. The CCD chip is supported by and thermally coupled to a copper frame. The copper frame has an electrically isolated thermal path to the cold reservoir via the braided copper strap.

frames and the filter materials were applied to the frames by the Luxel Corporation.

2.2. *Optics development*

The replicated optics fabricated at MSFC are electro-formed around a mandrel in which a prescription was single-point diamond turned into the surface, then subsequently polished to a fine specular finish. Similar to lapping techniques used in normal-incidence optical surface fabrication, X-ray mandrels are polished with cylindrical, concave lap tools that work on the surface in conjunction with various slurries and colloidal compounds. This process is effective for removing residual single point diamond turning tool marks and mid- and high-frequency figure errors, as well as for super-fine surface finishing that can readily achieve ≤ 5 Å root-mean-square (RMS) surface roughness. However, lap tools have a tendency to introduce low-frequency figure errors into the surface, with larger sag prescriptions suffering more.

Many of the nickel–cobalt replicated mirrors produced at MSFC yield point-spread functions (PSFs) with half-power diameter (HPD) angular resolution between 18–30″ (Gubarev *et al.*, 2014; Ramsey *et al.*, 2019; Champey *et al.*, 2019). Table 5 compares several grazing incidence telescope systems developed at MSFC that make use of nickel–cobalt replicated mirrors. Note that *MaGIXS* is a faster system (i.e. optical surfaces have larger sag, or curvature), with three additional reflective surfaces as compared to the other instruments listed. Imaging resolutions are listed for the fully integrated *MaGIXS* instrument, as well as for individual mirror performance measured from component level X-ray testing, which is discussed in Sec. 2.2.3.

2.2.1. *Deterministic CNC polishing*

Overcoming the fabrication challenges associated with the tight 6″ angular resolution requirement led to the pursuit of developing a robust process for refining mandrel surface figures. Both of the *MaGIXS* mandrels served as a pathfinder for deterministic polishing specifically tailored to correct low-spatial frequency figure errors, leading to high-resolution grazing incidence mirror mandrels. The process utilizes a *Zeeko IRP 600X* CNC polishing machine and is deterministic due to its ability to provide precise control of polishing tools that are guided by a meteorological feedback cycle (Gubarev *et al.*, 2016; Davis *et al.*, 2019). The process has demonstrated an ability to reduce low-frequency figure errors at spatial wavelengths > 7 mm. At shorter spatial wavelengths (< 5 mm), new tools must be developed to extend the response of the process into this range.

Figure 4 shows the before and after residual figure error on the paraboloid segment of the Wolter-I telescope mandrel and is the result of five polishing iterations with the *Zeeko* machine. The blue profile is the result of an axial profile measurement taken after removing residual diamond turning tool artifacts using a pitch-lined polishing lap. The green profile is from a measurement taken after the final figure correction pass. Only the features between 10–115 mm in axial position were addressed. The large deviations at the ends of the profiles were not corrected because they lie near physical edges on the mandrel that are avoided while polishing. The transition from the paraboloid segment to the hyperboloid segment is continuous, so the polishing tool can reach closer to this plane. Therefore, the avoided zone near the transition is

Table 5. MSFC-produced grazing incidence telescope systems.

Instrument [class]	Focal length [m]	# of Reflections	# Nested mirrors	HPD [arcseconds]
HEROES [Balloon]	6.0	2	12/13	25–30
ART-XC (SRG)[a] [Navigator (Russia)]	2.7	2	28	27.5
FOXSI [Sounding Rocket]	2.0	2	7/10	20
IXPE [Small Explorer]	4.0	2	24	22.5
MaGIXS [Sounding Rocket]	2.5[b]	5[c]	1	28–30
Telescope Mirror	1.1	2	1	16
Spectrometer Mirrors (×2)	0.63	1	1	17

Notes: [a]Spectrum-Roentgen-Gamma high-energy astrophysics observatory.
[b]Distance from entrance aperture to detector.
[c]Includes grating.

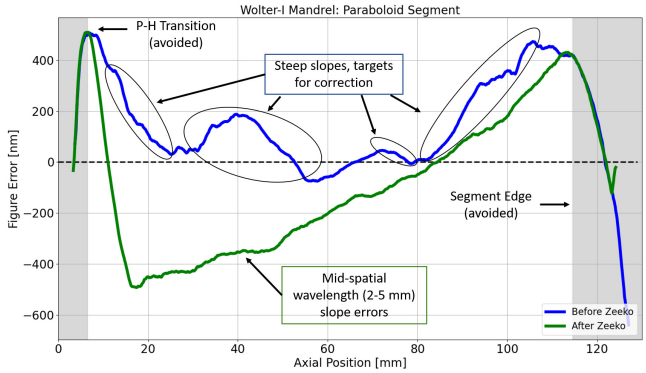

Fig. 4. Relative figure error of the paraboloid segment on the telescope mandrel. The before profile (blue) contained large amplitude, low-frequency slope errors. The after profile (green) shows the corrected surface that no longer contains the low-frequency errors (spatial wavelengths >7 mm). Still present, however, are mid-spatial wavelength (2–5 mm) errors that do not respond to the tools used in the process. The global positive slope in the green profile does not have a significant impact on performance, although it does translate to a small shift (<1 mm) in focal length of the telescope mirror.

~ 5 mm, whereas the avoided zone near the abrupt edge is ~ 15 mm.

The data shown in Fig. 4 are the relative figure error in linear units. However, the local slopes in the figure error at different spatial wavelengths were used as the metric to track corrections. Axial slope errors were reduced from $> 4''$ to $0.72''$ on the paraboloidal segment (Fig. 4), and from $> 6''$ to $1.26''$ on the hyperboloidal segment (Champey *et al.*, 2019). Including both the axial and azimuthal components of the figure errors, the combined RMS slope error of the region corrected on the mandrel are $1.0''$ and $1.55''$ on the paraboloid and hyperboloid segments, respectively. It is important to note that due to limitations imposed by the current metrology approach, the azimuthal figure error component was not addressed during this polishing effort.

2.2.2. *CGH null metrology*

The single paraboloid spectrometer mandrel surface figure was also corrected using the same deterministic process described above. However, a custom designed computer-generated hologram (CGH) null optic was used to supplement the metrology. The spectrometer mandrel prescription had $\approx 20\,\mu$m departure from a cone over an 80 mm segment, which was found to be near the limit for plane-wave interferometric metrology. Without the CGH, the fringe density was too large for the detector to resolve, which resulted in data dropouts. The CGH null operates in double pass and generates a test beam wavefront that matches the mandrel. The non-compensatable errors in this particular CGH is 45 nm peak-to-valley across the 4 inch aperture (in the azimuthal plane). The resulting interferogram is 3D surface error measurement of the mandrel with respect to the CGH phase function.

Figure 5 shows the relative figure error for the spectrometer mandrel before (blue) and after (green) employing the deterministic polishing process. The feature at $X = 16$ mm was unintentionally imparted into the figure during a series of prior lap polishing iterations. The deterministic polishing iterations removed enough material to generate a flat profile down to the bottom of the valley until further corrections became limited by the metrology accuracy. The axial RMS slope errors at 7 mm spatial wavelength were reduced from $3.0''$ (blue profile) to $0.4''$ (green profile). The slope near the edge of the mandrel ($X = 5$ mm) and the remaining valley ($X = 16$ mm) are the largest contributors to the RMS slope error. Similar to the green profile in Fig. 4, mid-frequency errors are also present.

One of the key components of the deterministic process is measuring and characterizing the 2D wear function (influence function) of the polishing tools. The wear function is well behaved and has little temporal variation, which makes it ideal for using as a fiducial to register the *Zeeko* machine with the mandrel and for tracking the wear rate of the surface between polishing iterations. The accuracy to

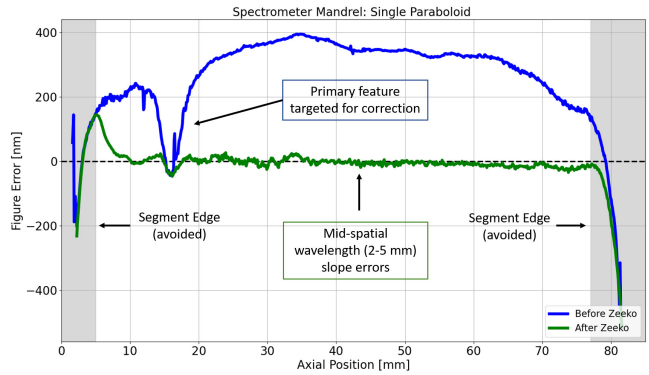

Fig. 5. Relative figure error of the spectrometer mandrel, measured with a CGH. The before profile (blue) shows a large valley at $X = 16$ mm. This feature was unintentionally imparted into the figure during a series of prior lap polishing iterations. The after (green) profile shows the corrected surface where much of the valley was corrected. Still present are mid-spatial wavelength errors similar to those seen in Fig. 4.

which the 2D wear function could be measured and tracked improved from 8.4 ± 4.1 nm without any null, to 2.2 ± 0.4 nm with the CGH null. This experiment demonstrated that supplementing metrology with a null optic yielded about a factor of four increase in accuracy of the registration between the mandrel and the *Zeeko* machine.

Note that a null optic was employed for the spectrometer mandrel, but not the telescope mandrel. The telescope mandrel prescription has less curvature and therefore was measured using plane-wave interferometry with sufficient accuracy for the process to be effective.

2.2.3. *Replicated mirror performance*

A key component of this development process was to determine if the error-corrected surface propagates through the process of replicating a mirror shell. A series of X-ray tests were designed to characterize the PSF and measure imaging performance as a function of pupil location. The three replicated grazing mirror were tested in the Stray Light Test Facility (SLTF) 100 m X-ray beam line at MSFC. An overview of the experiment design and preliminary on-axis PSF measurements are reported in Champey *et al.* (2019). In one test, the telescope mirror entrance aperture was masked and only allowed the active aperture (the portion of the aperture that would be incident on the grating) to image the point source. This provided a direct measurement of the on-axis PSF from the 34° active aperture. This masked aperture test was implemented when testing the TMA, but was not performed when testing the individual spectrometer mirror tests. Despite not having direct measurements of the PSF produced by the active aperture of the spectrometer mirrors, their full-width half-maxima (FWHM) and HPDs were obtained indirectly using out-of-focus images.

The out-of-focus images yield an annulus that is the far-field response of the exit pupil of the mirror. Thus, the cross-section of the annulus at any given azimuthal angle is a component of the in-focus, on-axis PSF. Figure 6(a) is an X-ray image produced by the first spectrometer mirror where the CCD camera was placed 6 mm in front of the mirror's focal plane. The image was processed to remove the background and was filtered to suppress residual noise below a threshold. The 100° corrected sector, denoted in the image, shows an enhanced response and correspondingly a narrower annular width as compared to the remainder of the mirror. A pair of fiducials were affixed to the entrance aperture of the mirror (Fig. 6(b)) to verify clocking of the mirror in the X-ray image.

Figure 7 shows two profiles that are the result of integrating the annulus over azimuth range $\theta = 125°$ to $\theta = 225°$ at steps of $\Delta\theta = 5°$. The left panel shows the integrated profile obtained from the defocused image in the left panel of Fig. 6, while the right panel shows the integrated profile from a

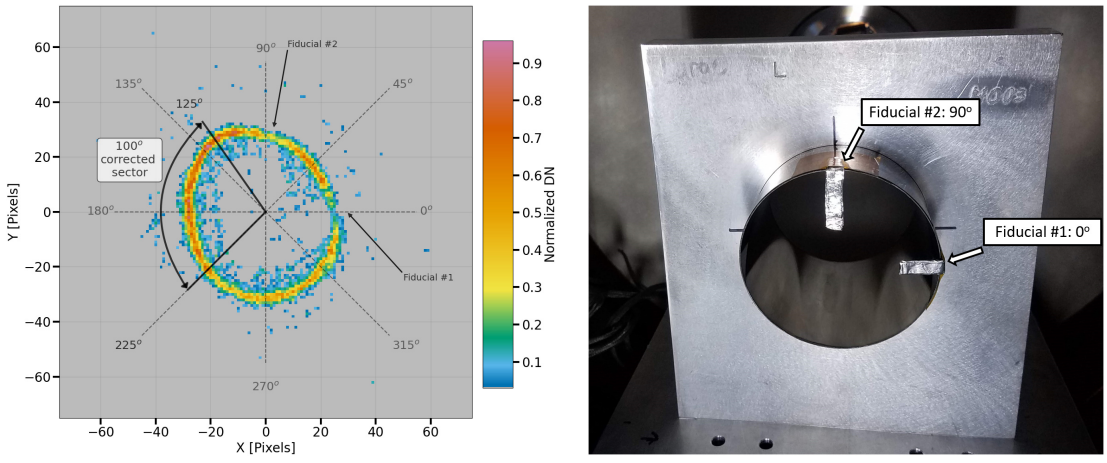

(a) (b)

Fig. 6. *Left:* An X-ray image produced by Spectrometer Mirror 1 (SM1) with the detector placed 6 mm inside of the mirror's focal plane. The sector bound by azimuth angles $\theta = 125°$ to $\theta = 225°$ had figure errors corrected via the deterministic polishing process. *Right:* SM1 in a test mount, looking at the entrance aperture from the direction of the source. Two fiducials were placed at the 0° and 90° locations that are meant to block X-rays, creating two shadows in the image that are used to register the clocking of the exit pupil.

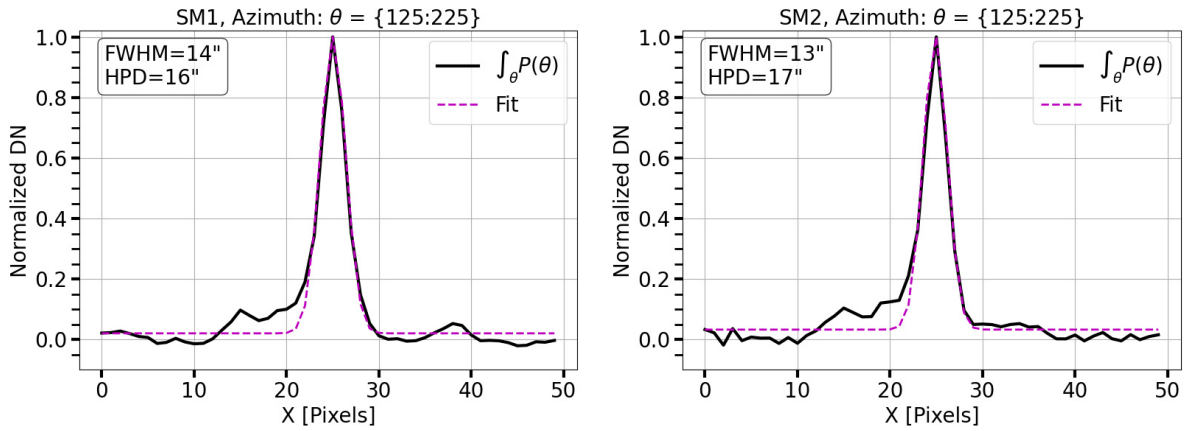

(a) (b)

Fig. 7. The integrated profiles (azimuth range $\theta = 125^\circ$ to $\theta = 225^\circ$) from the 6 mm out-of-focus X-ray images. Panel (a) is the profile extracted form the image shown in Fig. 6(a) (out-of-focus image from SM1). Panel (b) is the profile extracted from a similar out-of-focus image from SM2. The plate scale = 4.35″/pixel.

similar defocused image produced by the second spectrometer mirror (not shown). These profiles are a close approximation to the on-axis, in-focus PSF generated by the sector of the annulus included in the integration. The profiles were fit with a 1D Gaussian function plus a constant background term. The FWHM $= 2.35\sigma$, where σ is the standard deviation of the Gaussian fit. The HPD is computed directly from the data by taking the cumulative sum in the $-X$ and $+X$ directions from the center of the profile peak. The corrected sector on the mandrel led to mirror imaging performance of FWHM $= 14''$ and HPD $= 16''$ for SM1, and FWHM $= 13''$ and HPD $= 17''$ for SM2. The average net improvement was a 9% reduction in FWHM, a 7% reduction in HPD and a 15% increase in throughput, as compared to the non-corrected remainder of the mirror.

In both Figs. 7(a) and 7(b), the profiles have a feature at the base of the peak that begins at $X \approx 10$, but does not appear on the opposite side. The source is photons scattered in the radial plane (normal to the annulus) and the asymmetry is due to the fact that pixels that lie interior to the annulus detect a larger fraction of the annulus than pixels that lie exterior. This does have an impact on the HPD measurement. A more detailed analysis of out-of-focused images that considers this scattering behavior and pupil aberration will be discussed in a future paper (Champey *et al.*, in preparation).

The same analysis was performed on an out-of-focus image produced by the telescope mirror (Champey *et al.* (2019), Fig. 6(a)), which determined the corrected 100° sector on the telescope mirror performed with a ≈40% increase in throughput and ≈20% decrease in the FWHM as compared to the remainder of the mirror. The resulting imaging performance measured from the error corrected sector seen in the out-of-focus image was FWHM $= 12''$ and HPD $= 16''$. For comparison, in Champey *et al.* (2019) Fig. 5(b), the masked PSF image shows a preliminary HPD $= 14''$. The same image has since been reprocessed to remove residual noise and the cumulative sum was recomputed over a larger, 50×50 pixel region. The resulting HPD $= 16''$.

2.3. *Instrument layout and mechanical design*

The *MaGIXS* system is divided into four sub-assemblies — the Telescope Mirror Assembly (TMA), the Spectrometer Optical Assembly (SOA), the CCD camera assembly, and the secondary slit-jaw (SJ) imaging system for context imaging. Figure 8 is a rendering of the instrument CAD model that illustrates the system layout and the mechanical design.

2.3.1. *Optical bench*

The optical bench is composed of three 17-4 PH H1100 stainless steel tubes, with welded 17-4 PH H1100 flanges. The tube and flange assemblies were precision machined in a single operation to meet tight flatness and parallelism tolerances between opposing flanges. Each of the optical bench interfaces utilizes a pair of pins, which allows for simple and repeatable reassembly during the alignment

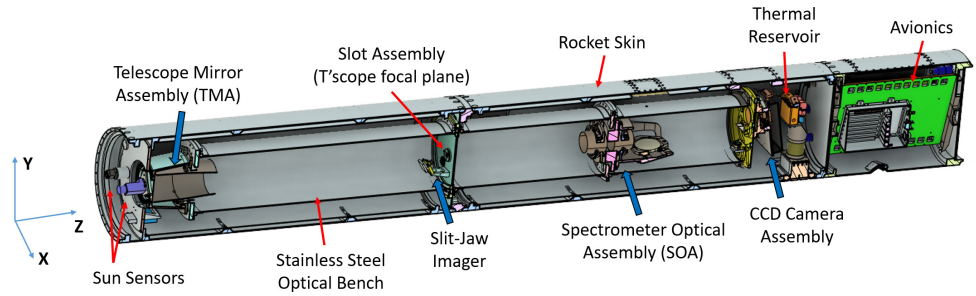

Fig. 8. The *MaGIXS* instrument mechanical layout. The 17-4 stainless steel optical bench has a single mechanical interface to the sounding rocket skin, located near the slit plane (image plane of the Wolter-I telescope). The TMA, SOA, and detector assembly are all supported by the optical bench.

process. The same is true for the interfaces between the optical assemblies and the optical bench. The TMA, SOA, and camera interfaces have 6-point mounts, where combinations of spacers and shims are used to adjust focus, tip, and tilt.

17-4 PH H1100 was selected as the material for the optical bench due to its thermal and structural properties. Instrument level dynamic analyses assessed the performance of the design in both flight and test environments. The analyses demonstrated that the design performed with adequate margin in the flight environment defined by the sounding rocket handbook (SRPO, 2015) and the deflection of the optical bench under gravity (a 1-G lateral (X, Y) load) during ground testing was adequate for alignment and calibration.

2.3.2. *Optics assemblies*

Optical alignment and mounting of the mirrors and grating were performed at SAO. A thorough description of the TMA and SOA alignment and assembly process are reported in Hertz *et al.* (2020). The single shell Wolter-I optic is supported on a titanium mounting flange and is attached by six titanium flexures via nickel bonding pads, as shown in Fig. 9. The nickel pads and titanium flexure material were selected for their close coefficient of thermal expansion (CTE) match to reduce thermal distortions to the optical surface. The TMA carries a cross-hair reticle, which lies at the center of the TMA aperture, and a flat reference mirror bonded to a cutout in the titanium mirror mounting flange. The mounting interface to the optical bench is designed to be adjustable, allowing for focusing and tip/tilt corrections. The interface also has a pair of dowel pins that mate with an over-sized hole and slot, which allows lateral translation across the interface, and increases the tip and tilt adjustment stroke. After the alignment is complete, the over-sized holes are filled with epoxy, encapsulating the pin and setting the alignment.

Also included in the TMA is the telescope mirror cover, which serves a dual purpose for protecting the mirror and supporting the entrance filters, reticle, and sun sensors. The reticle lies at the center of the cover and is aligned to the optical axis of the mirror - this process is discussed in Sec. 3.2. The sun sensor mounts to the mirror cover via a 3-point mount adapter plate. Prior to launch, the angular offset of the sun sensor to the TMA is measured using a theodolite and subsequent adjustments are made by inserting shims between the adapter plate and mirror cover interface.

The spectrometer mirrors are held individually using the same mounting design as the TMA, but with only three flexures and nickel bonding pads. As illustrated in Fig. 10, the individual mirror assemblies attach to opposite sides of the SOA interface plate. The grating is mounted to its own titanium

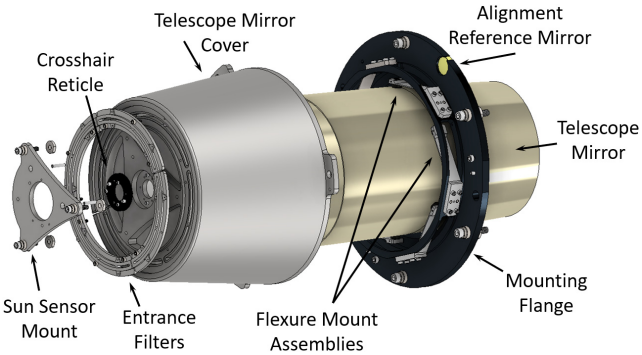

Fig. 9. The telescope mirror assembly (TMA). The telescope mirror is bonded to six tangential flexures with nickel pads and is supported by a titanium mounting flange. A mirror cover on the front side of the mirror supports the entrance filters, the cross-hair reticle alignment reference and the sun sensor mount.

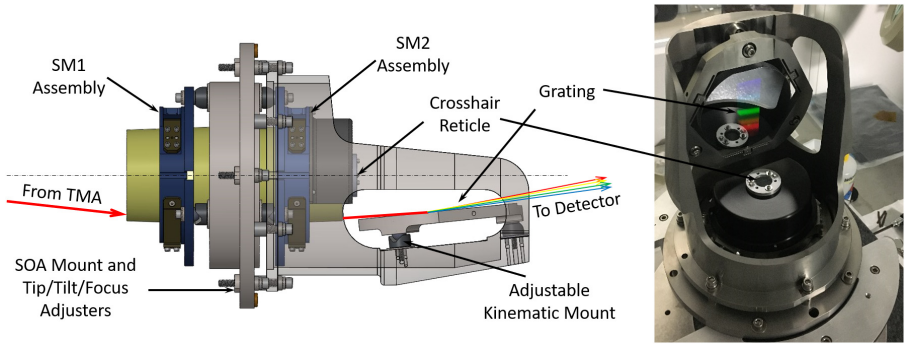

Fig. 10. The spectrograph optics assembly (SOA). The spectrometer mirror pair and the grating assembly attach to a common interface flange. The spectrometer mirror pair mounts and grating mount all have an adjustable mechanical interface to aid in their respective alignments.

structure and is also attached using a flexure and bond pad system. The grating mount fits over the SM2 mounting flange and attaches directly to the SOA interface plate. Like the TMA interface design, SM1, SM2 and the grating mounts are designed to be adjustable for focusing and tip/tilt corrections and then the alignment is locked into place by encapsulating the dowel pins with epoxy.

2.4. *Slit-jaw imager*

The *MaGIXS* slitjaw imager (SJI) design includes a metallic slot plate positioned at the focus of the Wolter-I telescope mirror and a simple visible light re-imaging assembly. The slot plate is coated with a phosphor extreme ultraviolet (EUB) to visible light conversion material, and the re-imaging assembly is composed of a commercial off-the-shelf lens and low-light camera (Vigil *et al.*, 2021). Because of the low sensitivity of the phosphor coating to soft X-rays, the entrance filters installed for flight were designed to pass EUV photons to the telescope that were then focused onto the slot. During calibration, the SJI aided in pointing the instrument toward the X-ray point source. The camera is sensitive to visible light and therefore was capable of tracking the image of the guide laser focused by the TMA. Figure 11 shows the SJ view of the slot used for calibration at the X-ray Cryogenic Facility (XRCF) (Calibration II, Fig. 2) fully illuminated with white light as well as examples of the visualization of the guide laser while pointed on and off the slot. The system was effective in determining the pointing orientation when performing X-ray tests with the slot and hole array reported in Sec. 3.5. The *Python*-based pointing and visualization software were tested during calibration, which helped to develop the final version used for flight.

2.5. *Avionics*

The *MaGIXS* avionics unit consists of a Data Acquisition and Control System (DACS), low noise power supply, signal conditioning and a vacuum gauge. The avionics system is designed to be modular so that it can be easily reconfigured to operate with MSFC developed camera systems, context imagers, and payload sensors. The avionics system for *MaGIXS* was re-purposed from *Hi-C 2/2.1*, with a few minor changes to the configuration and a new

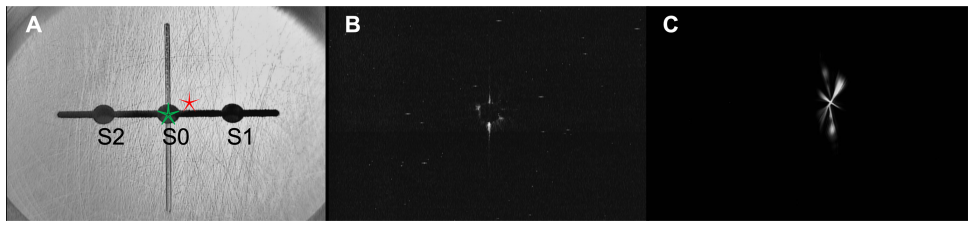

Fig. 11. Slit-jaw images obtained during X-ray testing at the XRCF. (A) Modified slot fully illuminated with white light. Positions along the slot, S2, S0 and S1 are labeled and correspond to results shown in Fig. 18. (B) Edges of the guide laser illuminates edges of slot at position S0. (C) Guide laser image is fully visible while pointed off of the slot. The locations of the guide laser pointed on the center of the slot and off the slot relative to the fully illuminated slot are shown (green and red star, respectively).

mount to fit into the 17 inch diameter skin section. A detailed description of the avionics system is given in Rachmeler *et al.* (2019).

3. Integration, Alignment and X-Ray Testing

3.1. *Alignment error budget*

The principal challenge for *MaGIXS* was co-aligning each of the five grazing incidence elements in series, displaced along the optical axis. A sensitivity analysis was performed on the optical system to assess the influence of various misalignment terms on the system's imaging and spectral performance (Champey *et al.*, 2016). The process included perturbing single components, e.g. each of the three mirrors and grating individually, and the spectrometer as a sub-assembly (SM1, SM2 and grating). Using *Zemax OpticStudio* ray tracing software, pitch, yaw, de-center and defocus misalignment terms were introduced into the model, and the resulting RMS spot radii, shift in dispersion on the detector, and fractional vignetting were evaluated as the figures of merit for system performance. The results of this study were used to construct an alignment error budget and to derive opto-mechanical tolerances for the optics mounts and optical bench. The most critical alignment in the system is the relative tip and tilt between SM1 and SM2 mirrors. This needed to be controlled within 5″ in order to keep off-axis aberrations minimized and avoid vignetting. In general, the relative alignment between the three spectrometer optics (SM1, SM2, and the grating) have the largest influence on system performance. A table comparing alignment tolerances derived from the error budget with as-built values is provided in Hertz *et al.* (2020), Table 1 therein.

3.2. *Grazing incidence mirror mounting*

The strategy for aligning the *MaGIXS* system was based on first locating the optical axes of each grazing incidence mirror and then aligning it to a pair of optical references. Each mounting flange carries a double-sided 19 mm diameter precision flat reference mirror and a positive reticle (cross-hair) that serves as a reference for centering of the optical axis in X, Y (Sec. 2.3.2).

Grazing incidence mirror to flange alignment was performed in a vertical orientation; the optical axes of the grazing incidence mirrors were parallel with the gravity vector. During setup, a *Wilde T3000* auto-collimating theodolite was co-aligned to the optical axis of the Centroid Detector Assembly (CDA) (Glenn, 1995). The theodolite was used to sight the reference mirrors on the mounting flanges. The mounting flanges were subsequently adjusted for tip and tilt using micrometers until the reference mirrors were brought into alignment with the theodolite, and therefore the CDA test beam. Micrometers were also used to translate the flanges laterally in X, Y and bring the reticle into alignment with the optical axes of the CDA test beam. The grazing incidence mirrors rested on a separate 5-axis fixture that allowed for tip/tilt, X, Y translation, and focusing. After both mounting flanges and the grazing incidence mirrors were aligned with the CDA, the mirror was bonded in place. The end result of this assembly step was an accurate knowledge of the position of the optical axis for each of the grazing incidence mirrors with respect to the references located on the mounting flanges. More details and measurements from the *MaGIXS* grazing incidence optics mounting and alignment process are given in Hertz *et al.* (2020).

For an infinite conjugate grazing incidence mirror (telescope with object at infinity), the system operates in double pass and the CDA is placed at the focus of the mirror. The CDA emits a blue-light (488 nm) pencil laser beam that is steered in a circumferential pattern around the annular aperture of the mirror under test. The beam reflects off of the test mirror surface and exits through the front (entrance aperture). The beam is then incident on a flat mirror and is reflected back through the test mirror, returning to the CDA. In the case of a finite conjugate system (i.e. the SM1 and SM2 spectrometer mirror pair), the CDA operates in single pass mode, with the CDA placed at one focus and a satellite camera placed at its conjugate. In either configuration, the camera detects the focused spots from the test beam and calculates their centroids. The distribution of these centroids at the detector plane is a trace of the mirror's PSF.

Figure 12 provides CDA outputs from a single scan of the aligned spectrometer mirror pair. Each point marks the centroid of the focused test beam, and the colorized vector bridging each point indicates the direction of the scanning beam, as well as the azimuthal position in annular aperture.

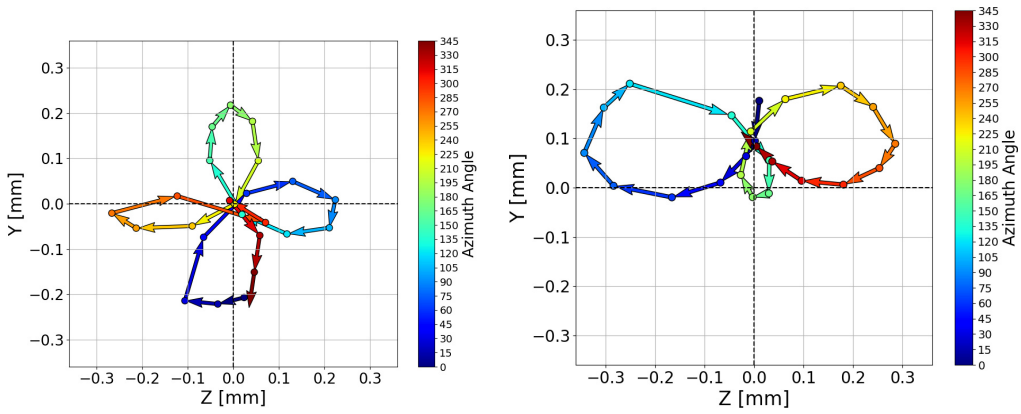

Fig. 12. CDA scans of the aligned SM1 and SM2 pair. (a) is a CDA scan of the mirror pair that was aligned to produce a symmetrical, minimized RMS spot size. (b) is a CDA of where the mirror pair was preferentially aligned to produce a minimized spot over the sub-aperture that is dispersed by the grating.

Figure 12(a) shows a balanced alignment between SM1 and SM2, where the RMS spot diameter was minimized over the full aperture. Figure 12(b) shows a preferential alignment between SM1 and SM2 that minimized the RMS spot size for the error corrected sub-aperture between azimuth angles 125° to 225° that falls onto the grating (see Sec. 2.2.3, Fig. 6(a)). This alignment solution for the mirror pair was the desired aligned state of the SM1 and SM2 pair.

3.3. *TMA and SOA focusing*

System integration and alignment were completed over several steps that began with focusing the TMA with the slot plane. The full system, TMA and complete SOA, were aligned on an optics table in the XRCF 10 k clean room. Throughout this phased integration and alignment process, a total of 17 X-ray tests were completed, and the data from these tests provided confidence and useful feedback to the indirect optical alignment techniques being performed.

3.3.1. *TMA focusing*

The first objective was to locate the on-axis focal plane of the TMA. The TMA was mounted to the telescope section of the optical bench, which was supported by the skin interface plate (SIP). The reference mirror on the TMA was aligned to the reference mirror on the SIP using the theodolite for measurement and shims at the mounting interface for adjustment. In place of the slit was a CCD camera that detected the X-ray image from the TMA. The TMA was translated in the focal direction (Z-axis) to produce intra- and extra-focused annuli, from which HPDs were calculated.

Figure 13 shows the measurements from the TMA integrated with the optical bench (red "+" markers) and measurements from a standalone TMA test in the SLTF, prior to integration with the optical bench (black circles). A pair of lines were fit to the SLTF data (gray dashed lines) and the intersection of these two lines imply the location of best focus (smallest spot size). The corresponding shift in focus (Δf) for the XRCF HPD measurements was solved using the linear fits from the SLTF data. With the shift in focus known relative to the best focused spot, the proper shim thickness was determined for focusing the TMA with the slot for ground testing (finite source distance). Then by applying the thin lens equation, the flight (infinite source distance) shim thickness was determined.

3.3.2. *TMA-SOA focusing*

Focusing the SOA followed the same approach as TMA focusing. With the TMA integrated to the optics bench, the SOA (without the grating) was mounted to the optics bench and a CCD camera was mounted on-axis near the SOA focal plane. The distance (front focus) of the SOA from the TMA focal plane was determined from the CDA measurements and was controlled with a set of spacers. The CCD camera was placed at an intentionally out-of-focus position to image the TMA and the SOA combination. The camera was subsequently shifted to a position on the opposite side of the SOA

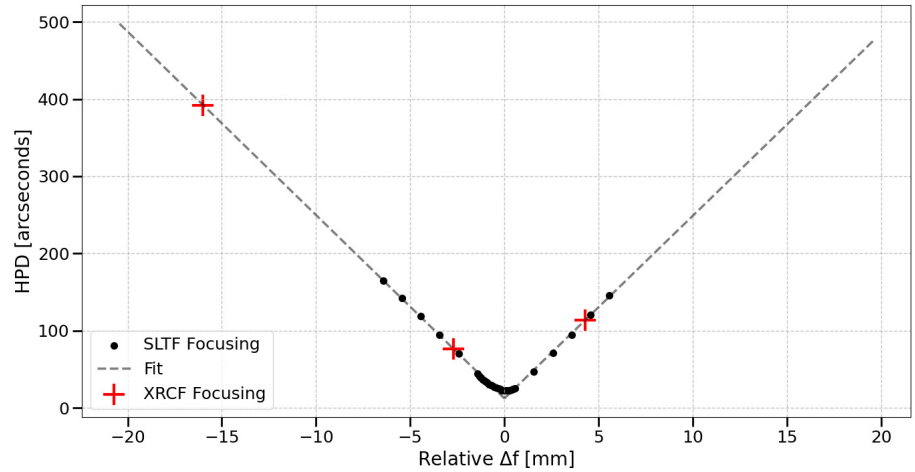

Fig. 13. TMA half-power diameter at relative defocus positions. The black circles are half-power diameters determined from TMA X-ray tests in the Stray Light Test Facility. The gray dashed lines are two separate fits to the data shown as the black circles and the intersection of these two lines implies the location of the best focused position. The red "+" markers are the HPDs measured from TMA tests in the X-ray Cryogenic Facility beam line. From these combined data, the shim sizes required to focus the TMA with the slot were determined for both ground testing (finite source) and flight (infinite source) configurations.

focal plane and a second out-of-focus image was captured. Using the same technique described in Sec. 3.3.1, the distance to the on-axis focal plane of the TMA-SOA combination was determined.

3.4. *System alignment approach*

The TMA and SOA are confocal at the slot plane and are separated by a span of 1.6 m, as shown in Fig. 14. The TMA, the slot at the TMA focal plane, and the SOA were to be precisely aligned using the reference mirrors and reticles located on each of the three sub-assemblies. The series of alignments described below were performed on an optics table and in the field before and after vibration testing.

3.4.1. *Alignment setup*

Using the references on the TMA and SOA, the relative alignment of the assemblies was measured with a theodolite and a pair of external flat mirrors placed on a laboratory optics table. The flat mirrors

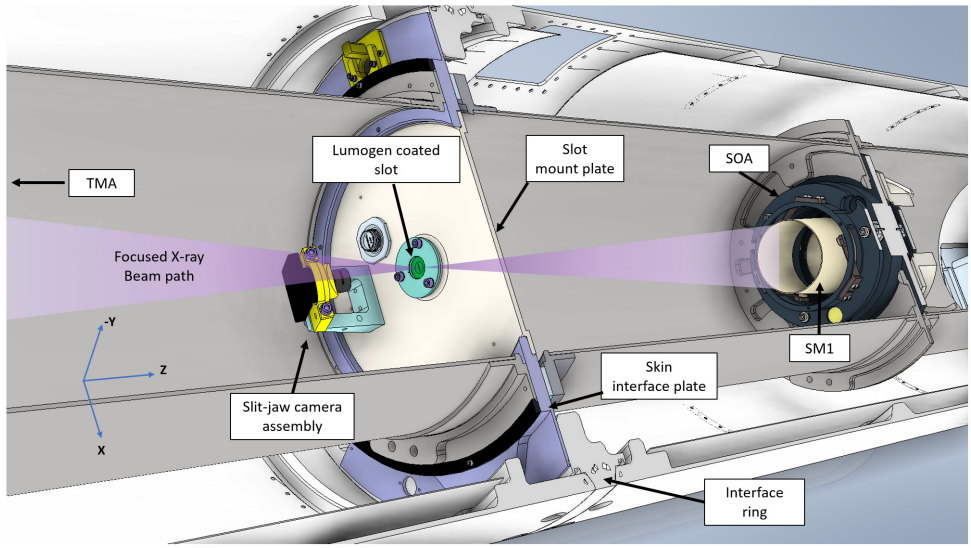

Fig. 14. The instrument CAD model showing a detailed view of the TMA focal plane and entrance to the SOA. The X-ray beam focused from the TMA is incident on the slot and is imaged by the Slit-jaw camera. After passing through the focal plane, the beam diverges and enters SM1 where it is collimated then re-focused by SM2. The principal challenge during integration was aligning the TMA and SOA and ensuring the optical axes of the two sub-assemblies were centered with the slot.

were designated as the transfer surface (12-inch diameter flat mirror) and the absolute reference (4-inch diameter flat mirror). Both mirrors were flat within $\lambda/20$ (32 nm) peak-to-valley. The theodolite was mounted to a 2-axis translation stage, which was required for the theodolite to be repositioned in order to sight targets at various X, Y positions. Figure 15 shows the placement of the theodolite, absolute reference, and the transfer surface, all with respect to the instrument. The 4-inch diameter absolute reference was positioned between the theodolite and the instrument and placed at a X, Y location such that when the instrument was rolled 180°, the mirror did not obstruct any of the line of sights of the theodolite to the reference mirrors in the instrument. The transfer surface was placed near the rear of the instrument and was tilted toward the theodolite. This surface was strategically placed so that it could be sighted by the theodolite at the X, Y positions dictated by the line of sight of each target - this was a requirement of the test.

Since the reference targets are not co-located, the theodolite must be translated and realigned to sight each of the targets. However, in moving the theodolite, all spatial reference is lost and the two independent measurements no longer have any meaningful relationship. The purpose of the transfer surface is to serve as a common plane that is used to compare measurements of two independent, non-co-located surfaces. In addition, the absolute reference is an external reference that serves as a global reference plane between the set of measurements obtained in the 0° and 180° orientations. The measured plane of the absolute reference is subtracted from the measured planes of the reference targets and transfer surface, tying each measured surface to a global reference.

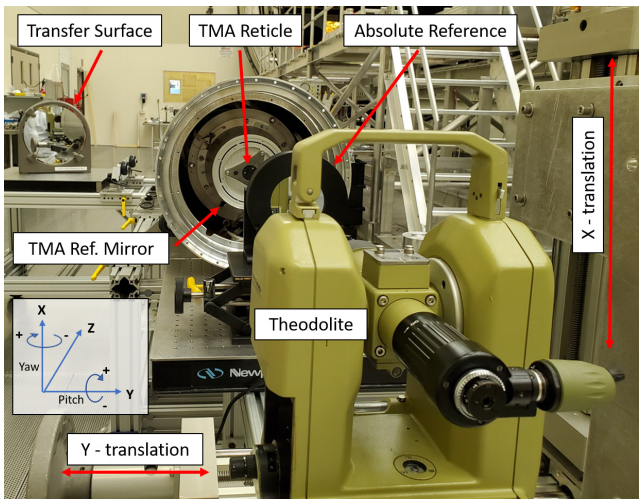

Fig. 15. The theodolite alignment setup for measuring the TMA and SIP reference mirrors. The theodolite is an auto-collimating *Leica Wilde T3000* model, mounted to an X, Y translation stage. The relative placement of the absolute reference and the transfer surface is required so that the absolute reference does not move between measurements taken at 0° and 180° orientations. It is also required that the theodolite must sight the transfer surface at each X, Y position dictated by theodolite line of sight for each target.

3.4.2. *TMA-SOA alignment*

The plane of each reference mirror was measured and recorded in a spreadsheet. Each data point consists of an angular measurement in the "horizontal" axis (yaw), and "vertical" axis (pitch) of the target surface. With the theodolite fixed in the X, Y plane, the theodolite is slewed back and forth between the reference mirror and the transfer surface, producing a pair of measurements for both surfaces. The difference between successive measurements is computed, then averaged. The process is repeated for each target, and then repeated again for all targets with the instrument rolled 180°. Rolling the instrument is a technique used to quantify and remove any contribution from the mechanical structure deflecting under a 1-G gravity load. Deflection measurements under a 1-G load are given in Table 6.

Figure 16 shows a schematic of how each reference was measured and provides a top view of the measurement layout. Each dashed line represents a line of sight of the theodolite when recording measurements. In Fig. 14, the skin interface plate is a solid surface, so there is no line of sight to the SOA reference mirror when looking boresight from the TMA end of the instrument. To measure the SOA, the instrument was flipped so that the theodolite had a line of sight with the SOA reference mirror, and the back side of the SIP reference mirror. The SIP reference mirror serves as a transfer and allows for direct comparison of the angular offset between the TMA and SOA reference mirrors.

Table 6. Deflection of the TMA and SOA under a 1-G load (mean $\pm 1\sigma$, sample size, $n = 10$).

Assembly	Yaw angle [arcseconds]	Pitch angle [arcseconds]
TMA	46 ± 15	38 ± 4
SOA	49 ± 15	30 ± 14

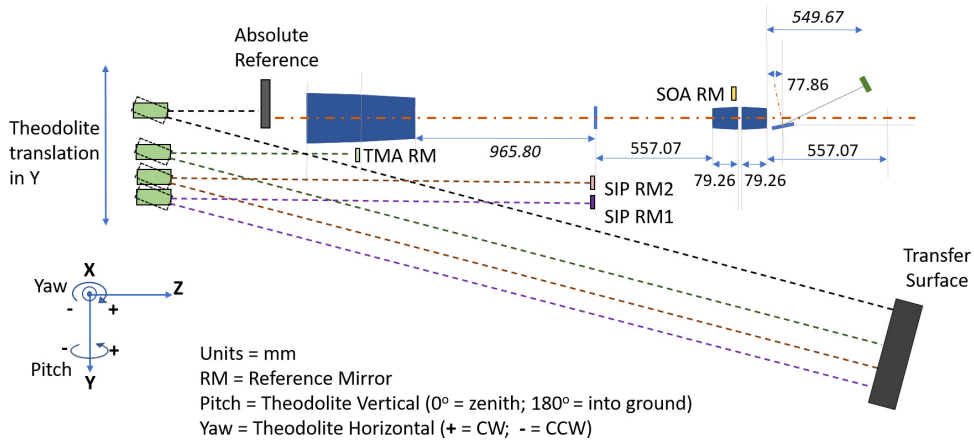

Fig. 16. Top view of the alignment setup. The dashed lines represent the line of sight of the theodolite as it sights the various target. The reference mirrors used to align the optics sub-assemblies are labeled as "RM."

Using the same setup in Fig. 16, the linear offset of the three reticles (TMA, SIP, and SOA) was measured and corrected. The process was similar to what is described above except that the reticles are printed onto a transparent fused silica substrate, so auto-collimation does not come into play. When looking boresight down through the TMA reticle, adjusting the focus of the theodolite eyepiece brings the downstream SIP and SOA reticles into sight. Initially, the theodolite was positioned such that the eyepiece reticle is centered on both the TMA reticle and the SIP reticle (i.e. the optical axis of the theodolite pierces the centers of both reticles). The X, Y position of the theodolite remained fixed and the theodolite angular position was recorded, along with the angular position of the transfer surface. Next the theodolite was returned to line of sight established for the TMA and SIP reticles and was re-focused bringing into view the final SOA reticle. The theodolite was slewed, centering the eyepiece on the SOA reticle, and the angular position of this line of sight and the location of the transfer surface was recorded. Applying the distances between the theodolite axis of rotation and the three reticles, the offset in X, Y (decentering) was calculated. This measurement procedure was repeated twice – once at 0° roll angle, and again at 180° roll angle. The deflection of the system due to the 1-G load was compensated in the centering adjustment. The end result was in both 0° and 180° orientations, the net centering offset in the vertical axis (parallel to gravity) was equivalent to the measured 1-G deflection. During flight, when gravity is off loaded, the system would move into alignment.

The tip/tilt error and decentering of the sub-assemblies were corrected at the SOA mounting interface to the optical bench. A set of three shims were machined and polished to within 10 μm and placed at three of the six fastener locations. The other three fasteners also had custom spacers machined but were installed after the alignment of the assembly was set. The de-centering of the two sub-assemblies was corrected via a pair of centering fixtures that used fine thread pitch adjusters. The fixtures were placed over the SOA mounting interface, with the outer ring attached to the optical bench flange and an inner ring attached to the SOA. The adjusters, located on the outer ring, pushed against the inner ring, allowing for precise, in-plane lateral translation of the assemblies across the bolted interface.

The left panel in Fig. 17 shows the evolution from the initial mounting of the SOA to the optical bench (red marker), to when the system was aligned. The first correction attempt (orange marker) reduced the error in pitch significantly, but doubled the error in yaw, indicating the misplacement of a shim. The pre-calibration measurements (pink markers) are measurements taken after alignment was complete, but prior to the XRCF calibration tests. From pre- to post-calibration (green markers), a shift was observed in the measurements of the relative alignment between the TMA and the SOA (yaw $\approx 0.6'$, pitch $\approx 0.8'$). The cause of this shift is not known. The right panel of Fig. 17 is rescaled to show the cluster of TMA to SOA alignment measurements taken post-calibration. The co-variance confidence ellipses are shown as green, blue and red dashed lines, representing 1,

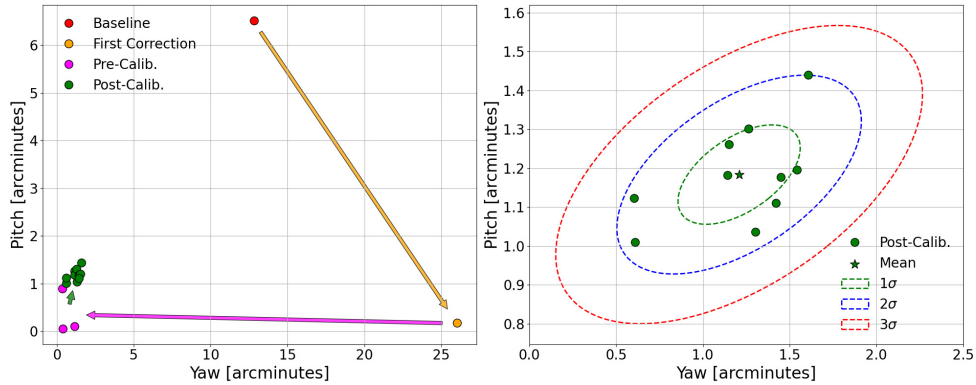

Fig. 17. The TMA-SOA alignment. Each point is a theodolite measurement of the TMA and SOA reference mirror offset. The left panel shows the evolution from the initial mounting of the SOA to the optical bench, to when the system was aligned. The right panel is rescaled to show the cluster of TMA to SOA alignment measurements taken post-calibration. The 1, 2, and 3σ confidence ellipses are plotted for the post-calibration measurements.

2, and 3σ confidence levels, respectively. Each individual green marker is measurement that was taken after the alignment between the TMA and SOA was broken (to change test configuration) and then realigned.

3.5. *End-to-end X-ray test*

End-to-end X-ray tests were performed in the XRCF 500 m evacuated beam line. The XRCF's Manson source with Ni, Zn, and Mg anodes was used to generate X-rays, and the beam normalization detector (BND) was used to measure the source irradiance. The first series of end-to-end tests made use of a slot and hole array placed at the TMA focus. The slot was 10 mm long, and 0.38 mm wide and had three 1 mm diameter holes at the center (on-axis) and two on either side at $\pm 9.5'$ off-axis, as shown in Calibration II, Fig. 2 therein. This field stop was used in place of the slit at the TMA focal plane to help overcome difficulty pointing the instrument toward the X-ray source with the five-axis mount (FAM) inside of the vacuum chamber. A low X-ray count rate made real-time image feedback impractical with the smaller slit. The 1 mm diameter holes are much larger than the size of the focused spot from the TMA, so they do not block any focused photons from reaching the spectrometer.

Figure 18 shows a composite image of the focused spots from imaging three different source targets. The data have been processed to correctly include photons whose charge clouds were detected over multiple adjacent pixels. The image has been smoothed with a 3×3 pixel box kernel and the color bar units are photons per second. Wavelength dispersion is along the detector X-axis and the spatial (imaging) component is along the detector Y-axis. The first- and second-order spectra were detected for the Mg and Zn lines, with the second order Ni line falling just off the edge of the detector. There are three distinct spots along the Y- axis that appear for the Mg and Ni lines at the $-9.5'$, $0'$, and $+9.5'$ field angle locations (S2, S0 an S1, respectively). However, in the case for observations with the Zn target, data were collected for S0 position only. For these tests, the instrument roll angle was set such that the dispersion axis was perpendicular to the gravity vector. In Fig. 18, the Y-axis is parallel to the gravity vector.

3.5.1. *PSF characterization*

The PSF was evaluated using two approaches. In Calibration II, the PSF was fit with a 2D Gaussian function and the HPD was calculated from image data. The caveat to this approach is that along the dispersion axis, the spatial and spectral point spreading are coupled. Thus, integrating the focused spots along the dispersion axis is one way to suppress the influence of the spatial-spectral coupling and assess only the spatial component. The focused spots along the spatial axis in Fig. 18 were cropped and then summed along the X-axis. In the case of the Ni-Lα, β line pair, the image was cropped such that the Lα and Lβ spots were segregated. The result was a 1D profile along the spatial axis of the focused spots for each line species.

Figures 19(a) and 19(b), top panel, show the focused spots for the Mg-Kα**(1.25 keV)** and Ni-Lα **(0.85 keV)** lines extracted from Fig. 18

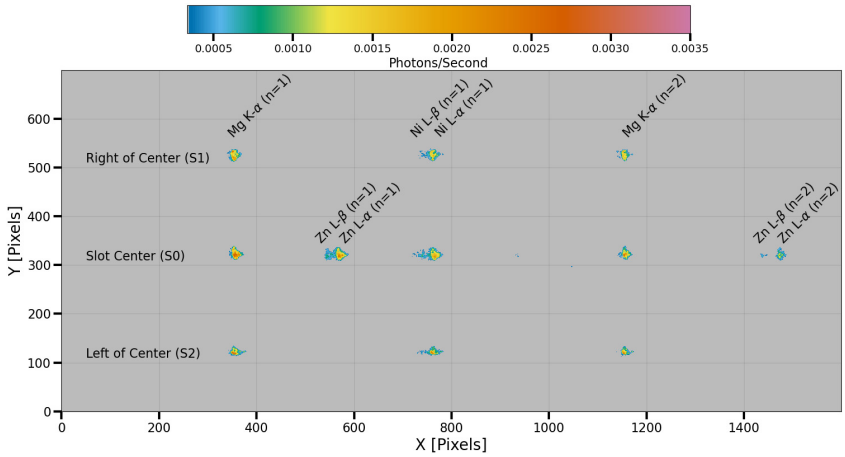

Fig. 18. The composite X-ray image containing all of the data collected from the fully integrated calibration tests. First- and second-order spectra were detected for the Mg-kα and Zn-Lα, β lines. The first-order Ni-Lα, β line is detected near the center of the image, with the second-order line falling just off to the right side of the detector.

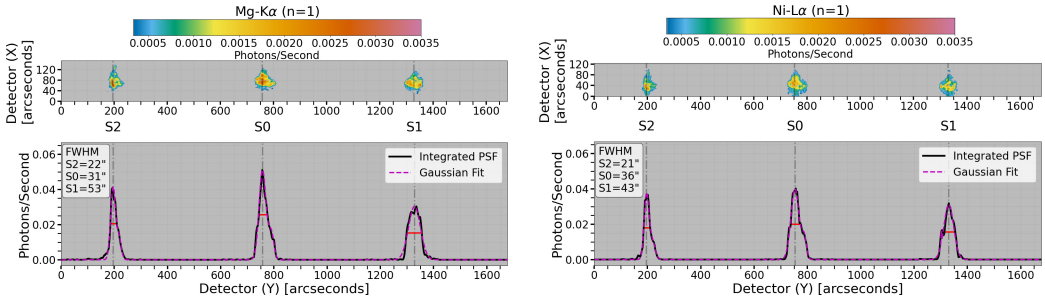

(a) (b)

Fig. 19. Images of the focused spots and PSF profiles for the Mg-Kα ($n = 1$) (left panel) and Ni-Lα ($n = 1$) (right panel). The PSF profiles are the result of integrating over the spots in the dispersion axis (Detector X-axis). A sum of two 1D Gaussian functions were fit to each of the three spot profiles and are over-plotted onto the profiles as the fuchsia dashed line. The vertical dashed-dot gray lines indicate the mean of Gaussian fit to the core, and the horizontal red lines denote the FWHM.

and rotated 90°. The bottom panels are the profiles of the spots integrated along the detector X-axis (dispersion axis), plotted as the black curve. Each of the spot profiles was fit with the sum of two 1D Gaussian functions (fuchsia dashed curves) from which the FWHMs are calculated (red solid lines). The FWHMs are listed in the text box in the upper left corner of the bottom panels.

The HPD was also computed from the integrated profiles at each field angle. HPD is calculated by taking the cumulative sum, centered at the peak of the spot's profile. In Fig. 20, the cumulative sum is plotted against radius from center of the peak for both Mg-Kα (20(a)) and Ni-Lα (20(b)) first order. Interpolation was used to calculate the width of the profile containing 50% of the total photon counts. The half-power-radius is indicated by the intersection of the black dashed line at 50% of the normalized power and vertical dashed lines for each curve. The HPDs shown in the legend of Fig. 20 are plotted against the field angle in Fig. 21.

The HPD of the spatial component of the *MaGIXS* PSF are plotted over the ±9.5′ field of view in Fig. 21. Included in the figure is the second-order Mg-Kα line and the range of predicted HPD obtained from component-level PSF characterization (gray box). The upper HPD limit is 31″ and was calculated by convolving the PSFs of the TMA and spectrometer mirrors (Champey *et al.* (2019), Fig. 8). The lower limit is 28″ and was estimated from the root-sum-square (quadrature sum) of the HPDs measured for the active apertures of the TMA and spectrometer mirror pairs (Sec. 2.2.3). The average HPD of the fully integrated instrument

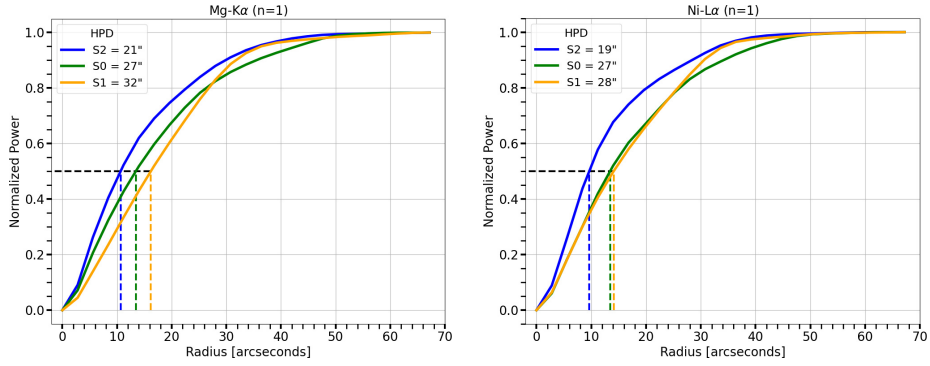

(a) (b)

Fig. 20. The cumulative sum of profiles in Fig. 19, for both Mg-Kα ($n = 1$) (*left* panel) and Ni-Lα ($n = 1$) (*right* panel). The HPD for each curve is indicated by the intersection of the dashed lines.

was 20″, 26″ and 30″ at the S2, S0 and S1 field positions, respectively.

The difference in HPD performance predicted from component-level X-ray tests and the measurements from the end-to-end X-ray tests are relatively small. The average HPD measured for the S1 position falls within the expected range, while the HPD at the S0 position falls just below the bottom of the range by a difference $< 10\%$ ($<$ one pixel).

Despite the agreement between S0 and S1 with the component level predictions, S2 shows a narrower spot and correspondingly smaller HPD. The cause of the variation in performance across the $\pm 9.5'$ field of view is not immediately understood and a follow up investigation supplemented with flight data is being performed. Discussed below in Sec. 4 is an observed misalignment between the optical axis of the TMA and the slot, which may be a contributor to this response in the performance. Preliminary results of the flight data imply the spatial resolution is consistent with the HPD measured at the S0 position, however the analyses are not complete. This issue will be probed more as the flight data is processed to a higher level and will be revisited in Savage *et al.* (2022).

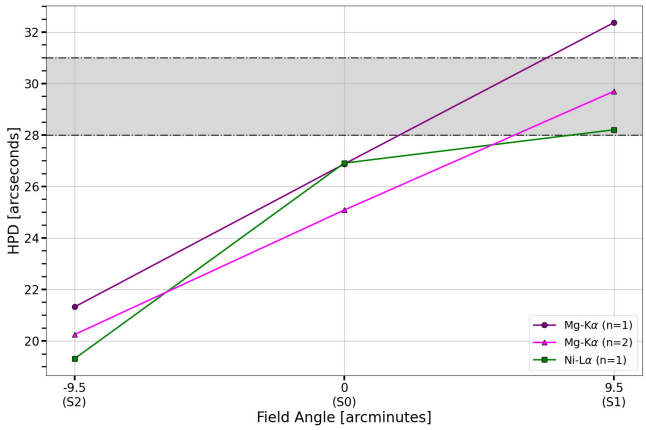

Fig. 21. HPD imaging performance for Mg-Kα ($n = 1$ and $n = 2$) and Ni-Lα ($n = 1$). The gray box bounded by the black dash-dot lines represents the range of HPD predicted from component level X-ray testing. The 31″ upper limit was computed by convolving the X-ray PSFs from the TMA and the spectrometer mirror pair. The 28″ lower limit was computed from the root-sum-square (quadrature sum) of the HPD measurements discussed in Sec. 2.2.3. A clear gradient in resolution is observed across the $\pm 9.5'$ field of view. The cause of this feature is being investigated further with the flight data.

4. Discussion

MaGIXS had a successful flight and recovery on July 30, 2021, detecting X-ray spectra of a pair of active regions near the western solar limb. The systems within the instrument operated nominally during flight, with avionics, CCD camera and SJ system not reporting any issues. The flight data show that comprehensive success criteria were met. A mission paper (Savage *et al.*, 2022) is in preparation and will discuss flight data processing, analysis, and initial science results.

However, during fabrication, integration and flight, several observations were made indicating the instrument was not in an optimal state. Changes from the original design, either due to choice or evolution of the design, fabrication limitations, and mistakes during assembly that impacted X-ray performance during flight are discussed.

4.1. *Large point spread function*

Despite the advancements in correcting figure errors via deterministic CNC polishing, the replicated mirrors did not meet the 6″ resolution goal. There

are known contributing factors that impacted the resolution. First, the Wolter-I telescope mandrel was damaged and repaired during a deterministic polishing operation. The 100° error-corrected segment was not part of the damaged area. Although, the underlying aluminum substrate is suspected to have been warped, causing non-circularity in the mandrel, which was observed as a hexafoil shape in the defocused TMA images reported in Champey *et al.* (2019).

Another contributor imparted stresses in the replicated mirrors that impact resolution. During replication, discontinuities in the electric field near the ends of the mirror segment cause figure errors that propagate ≈ 20 mm from the mirror edge into the focusing optical surface. There was no ability to measure or model this effect at the time the *MaGIXS* mirrors were produced, but results from more recent work indicates this is the dominate source of stress induced figure errors in the replicated mirror. In Sec. 2.2.3, observed improvements to the error-corrected mirror sectors are reported, but it is likely the imaging performance of the replicated mirror which is limited by these edge effects.

4.2. *Alignment issue*

Observations during ground testing suggest: An alignment issue between the optical axis of the system and the slot. Heliostat testing at the White Sands Missile Range, NM, implied that the image formed by the TMA and detected by the SJI was offset from the center of the slot by up to 9′. This offset was accounted for when pointing the instrument during flight. However, an preliminary analysis of the flight data suggests that while some alignment offset is detected in the observations, the alignment offset is less than 9′.

In retrospect, this issue was first detected when performing the TMA focusing X-ray tests. The test concluded that the on-axis focal spot of the TMA was offset from the center of the CCD that was in place of the slit (Calibration II). It was not realized that this result indicated an alignment offset between the TMA and the center of the slot. To correct for this issue, a tip and tilt adjustment at the TMA is needed to force the on-axis focus to the center of the slot. This could be done by repeating the TMA focusing test discussed in Sec. 3.3.1.

The apparent net effect is that *MaGIXS* operated at an off-axis field angle, potentially diminishing throughput and resolution. This was corroborated when revisiting the ray trace model and producing a field-dependent vignetting function. At the observed off-axis field angle, vignetting reduces throughput to $< 10\%$, which shows agreement with the measured effective area reported in Calibration II. This will be investigated further in Savage *et al.* (2022).

4.3. *Reduced throughput and change from slit to slot*

The original *MaGIXS* design included a 15 μm (2.8″) wide by 2.5 mm (8′) long slit. During the final assembly, the slit was exchanged for a 3.84 mm ($\sim$12 arcmin) wide by 10.6 mm (33′) long slot. There were two drivers for this design change. The first was the measured $\sim$80% reduction in effective area reported in Calibration II, which was likely due to the misalignment of the slit to the TMA optical axis. The second was the recent development of an overlappogram inversion algorithm (Cheung *et al.*, 2019; Winebarger *et al.*, 2019; De Pontieu *et al.*, 2020).

5. Conclusion

MaGIXS is designed as a sounding rocket instrument in response to a critical gap in solar soft X-ray observations. The requirements are to observe soft X-ray spectra of spatially resolved solar active region loops with simultaneous spatial (5″) and spectral (22 mÅ) resolution. Several challenges associated with meeting these goals propagated down to the grazing incidence optics fabrication and the alignment of the system. The Wolter-I telescope and the spectrometer mirror pair were the first set of mirrors to be replicated from a mandrel that underwent a CNC deterministic polishing process. The process was effective for correcting large-amplitude, low-frequency figure errors that led to improvements in replicated mirror performance. In addition, technical advancements in a direct-write process for dense, highly chirped line rulings led to successful grating fabrication. Lastly, the approach for indirectly aligning the grazing incidence mirrors from a series of references enabled repeatable alignment of optical assemblies on a laboratory optics table, and in the field. The synergy of these technologies, processes, and methods resulted in a well-executed *MaGIXS* instrument.

MaGIXS had a successful flight and recovery on July 30, 2021. During the flight, *MaGIXS* observed a pair of active regions on the western limb. These observations, in-flight performance and results will be presented in Savage *et al.* (2022), and other future works. Despite the unresolved issued discussed above, *MaGIXS* has demonstrated a revolutionary concept for grazing incidence imaging spectroscopy. The development of this concept is meant for far more than an single sounding rocket mission.

References

Athiray, P. S., Winebarger, A. R., Barnes, W. T. *et al.* [2019] *ApJ* **884**, 24, doi: 10.3847/1538-4357/ab3eb4.

Athiray, P. S., Winebarger, A. R., Champey, P. *et al.* [2020] *ApJ* **905**, 66, doi: 10.3847/1538-4357/abc268.

Athiray, P. S., Winebarger, A. R., Champey, P. *et al.* [2021] arXiv:2109.01720.

Champey, P., Kobayashi, K., Winebarger, A. *et al.* [2014] *Proc. SPIE* **9144**, 914439, doi: 10.1117/12.2057321.

Champey, P., Kobayashi, K., Winebarger, A. *et al.* [2015] *Proc. SPIE* **9601**, 96010Z, doi: 10.1117/12.2188754.

Champey, P., Winebarger, A., Kobayashi, K. *et al.* [2016] *Proc. SPIE* **9905**, 990573, doi: 10.1117/12.2232820.

Champey, P., Winebarger, A. R., Athiray, P. S. *et al.* [2019] *Proc. SPIE* **11119**, 1111917, doi: 10.1117/12.2532397.

Cheung, M. C. M., De Pontieu, B., Martínez-Sykora, J. *et al.* [2019] *ApJ* **882**, 13, doi: 10.3847/1538-4357/ab263d.

Christe, S., Glesener, L., Buitrago-Casas, C. *et al.* [2016] *J. Astron. Instrum.* **5**, 1640005, doi: 10.1142/S2251171716400055.

Davis, J., Champey, P., Kolodziejczak, J. & Griffith, C. [2019] *Proc. SPIE* **11119**, 111190U, doi: 10.1117/12.2532198.

De Pontieu, B., Martínez-Sykora, J., Testa, P. *et al.* [2020] *ApJ* **888**, 3, doi: 10.3847/1538-4357/ab5b03.

Del Zanna, G., Dere, K. P., Young, P. R. *et al.* [2015] *Front. Astron. Space Sci.* **582**, A56, doi: 10.1051/0004-6361/201526827.

Del Zanna, G., Andretta, V., Cargill, P. J. *et al.* [2021] *Front. Astron. Space Sci.* **8**, 33, doi: 10.3389/fspas.2021.638489.

Doschek, G. A. & Feldman, U. [2010] *J. Phys. B, At. Mol. Phys.* **43**, 232001, doi: 10.1088/0953-4075/43/23/232001.

Glenn, P. E. [1995] *Proc. SPIE* **2515**, 352, doi: 10.1117/12.212606.

Golub, L., Deluca, E., Austin, G. *et al.* [2007] *Sol. Phys.* **243**, 63, doi: 10.1007/s11207-007-0182-1.

Gubarev, M., Ramsey, B., O'Dell, S. L. *et al.* [2013] *Proc. SPIE* **8861**, 88610K, doi: 10.1117/12.2027141.

Gubarev, M., Ramsey, B., Elsner, R. *et al.* [2014] *Proc. SPIE* **9144**, 91441V, doi: 10.1117/12.2056813.

Gubarev, M., Kolodziejczak, J. K., Griffith, C. *et al.* [2016] *Proc. SPIE* **9905**, 99051V, doi: 10.1117/12.2233666.

Hertz, E., Cheimets, P., Hohl, J. *et al.* [2020] *Proc. SPIE* **11444**, 114448A, doi: 10.1117/12.2576145.

Kobayashi, K., Cirtain, J., Golub, L. *et al.* [2010] *Proc. SPIE* **7732**, 773233, doi: 10.1117/12.856793.

Krucker, S., Christe, S., Glesener, L. *et al.* [2013] *Proc. SPIE* **8862**, 88620R, doi: 10.1117/12.2024277.

Lemen, J. R., Title, A. M., Akin, D. J. *et al.* [2012] *Sol. Phys.* **275**, 17, doi: 10.1007/s11207-011-9776-8.

O'Dell, S. L., Atkins, C., Broadway, D. M. *et al.* [2015] *Proc. SPIE* **9510**, 951003, doi: 10.1117/12.2179415.

O'Dell, S. L., Baldini, L., Bellazzini, R. *et al.* [2018] *Proc. SPIE* **10699**, 106991X, doi: 10.1117/12.2314146.

Rachmeler, L. A., Winebarger, A. R., Savage, S. L. *et al.* [2019] *Sol. Phys.* **294**, 174, doi: 10.1007/s11207-019-1551-2.

Ramsey, B. D., Bongiorno, S. D., Kolodziejczak, J. J. *et al.* [2019] *Proc. SPIE* **11119**, 1111903, doi: 10.1117/12.2531956.

Savage, S., Winebarger, A. R., Athiray, P. S. *et al.* [2022] "The First Flight of the Marshall Grazing Incidence X-ray Spectrometer (MaGIXS)," in preparation.

Schmelz, J. T., Reames, D. V., von Steiger, R. & Basu, S. [2012] *ApJ* **755**, 33, doi: 10.1088/0004-637X/755/1/33.

SRPO [2015] *NASA Sounding Rockets User Handbook, Sounding Rockets Program Office, Sub-orbital and Special Orbital Projects Directorate*, https://sites.wff.nasa.gov/code810/files/SRHB.pdf.

van Speybroeck, L. P. & Chase, R. C. [1972] *Appl. Opt.* **11**, 440, doi: 10.1364/AO.11.000440.

Vigil, G. D., Winebarger, A. R., Kobayashi, K. *et al.* [2021] *Sol. Phys.* **296**, 90, doi: 10.1007/s11207-021-01834-0.

Warren, H. P., Winebarger, A. R. & Brooks, D. H. [2012] *ApJ* **759**, 141, doi: 10.1088/0004-637X/759/2/141.

Winebarger, A. R., Weber, M., Bethge, C. *et al.* [2019] *ApJ* **882**, 12, doi: 10.3847/1538-4357/ab21db.

Wolter, H. [1952] *Ann. Phys.* **445**, 286, doi: 10.1002/andp.19524450410.

Young, P. R. [2021] *Front. Astron. Space Sci.* **8**, 50, doi: 10.3389/fspas.2021.662790.